Advanced Materials

ADVANCED MATERIALS
www.advmat.de

RESEARCH ARTICLE

Spin-Orientation Modulation of Topology and Transport in a Breathing-Kagome Weyl Magnet

Yang Liu[1,2] | Junyan Liu[1] | Jiamin Mou[3,4] | Jinying Yang[1] | Meng Lyu[1] | Yibo Wang[1,2] | Subir Sen[1] | Xuebin Dong[1,2] | Xingchen Liu[1,2] | Binbin Wang[1] | Yuan Yao[1] | Xiyang Li[1] | Claudia Felser[5] | Defa Liu[3,4] | Enke Liu[1,2]

[1]Beijing National Laboratory For Condensed Matter Physics, Institute of Physics, Chinese Academy of Sciences, Beijing, China | [2]University of Chinese Academy of Sciences, Beijing, China | [3]School of Physics and Astronomy, Beijing Normal University, Beijing, China | [4]Key Laboratory of Multiscale Spin Physics, Ministry of Education, Beijing, China | [5]Max Planck Institute For Chemical Physics of Solids, Dresden, Germany

Correspondence: Defa Liu (defa.liu@bnu.edu.cn) | Enke Liu (ekliu@iphy.ac.cn)

Received: 27 May 2026 | **Revised:** 3 July 2026 | **Accepted:** 16 July 2026

Keywords: angle-resolved photoemission spectroscopy | anomalous hall effect | breathing kagome lattice | first-principles calculations | magnetic weyl semimetal | topology

ABSTRACT

The manipulation over diverse topological matters has become a critical demand for advancing quantum devices and topological spintronics. However, such experimental demonstrations remain scarce. Here, based on a novel breathing kagome magnetic Weyl semimetal $LaCrGe_3$, we realize a spin-rotation driven Weyl state evolution under the control of an external magnetic field. While the breathing of kagome lattice is revealed to boost the desired topologic state, the predicted Weyl points are observed around the Fermi level via angle-resolved photoemission spectroscopy, and are further corroborated by transport effects of chiral-anomaly-related negative magnetoresistance and large anomalous Hall conductivity. By rotating the external magnetic field, we demonstrated that the reorientation of magnetic moments can drive the motion of Weyl points in momentum space, which is characterized by a highly tunable angle-dependent Hall response. Our study presents a modulation of both topology and transport via spin orientation that offers fundamental insights for developing next-generation spin-based functional devices based on topological physics.

1 | Introduction

Achieving efficient control of topological electronic states through external fields serves as a critical foundation for emerging topological quantum devices and topological spintronics [1–3]. In a nonmagnetic topological crystal, the Weyl points are located at the fixed positions in momentum space, and their positions and energies cannot be changed easily [4]. The realization of coupling between magnetism and topology in metallic systems not only elevates the spin-dependent physical properties [5–8] but also establishes the external magnetic field as an effective knob for manipulating topological states through inherent magnetization. With magnetic moments reorienting and symmetry breaking, the electronic states normally show subtle alterations [9]. In magnetic topological materials, the dispersion of gapped nodal lines, the position of Weyl nodes, as well as the distribution of topological surface states, can be tuned by manipulating the magnetization vector through an external magnetic field. Consequently, magnetic-field-induced spin reorientation can modulate anomalous Hall and other

Yang Liu, Junyan Liu and Jiamin Mou contributed equally in this work.

transverse transport responses. This approach enables reversible control of the topological electronic structure without introducing additional disorder, thereby providing a promising basis for field-tunable topological spintronic devices and related functionalities that are sensitive to the Weyl-point positions near the Fermi level.

Research efforts are increasingly directed toward the feasibility of manipulating magnetic topological states via external fields. As a typical ferromagnetic Weyl semimetal with rich topological properties [5, 8, 10], $Co_3Sn_2S_2$ exhibits a giant anisotropic magnetic field of up to 23 T with its moments favoring out-of-plane axis [11]. The tunning of Weyl physics through the magnetization in this system is thus challenging. As a result, creating Weyl nodes and tuning their energy by the magnetization rotation in $Co_3Sn_2S_2$ have been only studied theoretically [12]. For topological antiferromagnet Mn_3Sn, the manipulation of topological states by magnetic field is much more difficult due to its tinny net moments and large magnetic anisotropy [13, 14]. A change of anomalous Hall effect via magnetization rotation induced by magnetic field is reported in ferromagnetic Weyl semimetal Co_2MnAl [15], which indicated the possibility of topology evolution driven by magnetic field, though there is no spectroscopic observation. Currently, the family of magnetic Weyl materials suitable for external field modulation remains limited.

Hence, the pursuit of new magnetic Weyl materials with attractive characteristics remains ongoing. The breathing kagome compounds RTX_3 (R = La-Nd, Sm; T = Transition metals; X = Group 13-15 elements) exhibit a rich diversity of crystal structures and a wide range of intriguing physical properties [16–24]. Recently, $CeCrGe_3$ was reported to exhibit giant anomalous Hall and Nernst effects [25], while $PrCrGe_3$ showed a skew-scattering-dominated large anomalous Hall effect [26]. These results indicate that this RTX_3 family may exhibit novel topological states and attractive physical properties.

In this work, combining electric transport and angle-resolved photoemission spectroscopy (ARPES) measurements with density functional theory (DFT) calculations, we establish $LaCrGe_3$ as a newly identified magnetic Weyl semimetal. Magnetotransport measurements reveal a large anomalous Hall effect in $LaCrGe_3$ and provide evidence consistent with a chiral-anomaly-related contribution to the negative magnetoresistance from Weyl fermions. Moreover, the chiral-anomaly-related negative magnetoresistance and angle-dependent anomalous Hall response, together with first-principles calculations, support a spin-orientation-dependent evolution of the Weyl electronic structure and demonstrate the tunability of the anomalous Hall effect through magnetic-moment rotation in $LaCrGe_3$.

2 | Topological Electronic Structures and Enhanced Anomalous Hall Effect

$LaCrGe_3$ crystallizes in the $BaNiO_3$-type structure with the space group of $P6_3/mmc$ (SG: 194) [27], as shown in Figure 1a. Each Ge atom layer forms a breathing kagome (BK) lattice with unequal Ge—Ge bonds bond lengths (left side of Figure 1c), as observed in *ab*-plane using the high-resolution electron microscopy (Figure 1b). La atoms occupy the centers of Ge hexagonal rings, while Cr atoms are positioned above the centers of Ge triangular rings (also see Figure S1b). Compared to the La—Ge bond, the Cr—Ge—Cr bond in $LaCrGe_3$ is a strong covalent bond and likely dominates electrical transport. This is consistent with the high electron occupancy probability obtained from the three-dimension electron localization function (Figure 1a), a result further supported by the difference charge density data (see Figure S1c). Additionally, the magnetization measurements reveal that $LaCrGe_3$ undergoes a ferromagnetic transition with a Curie temperature (T_C) of 85 K, and the magnetic moments of Cr tend to align along *c*-axis (the easy axis), as shown in Figure 1a. The saturation field is approximately 0.02 T along *c*-axis while 4 T along *ab*-plane at $T = 2$ K (see Figure S2).

The electronic structure and topological states of $LaCrGe_3$ were comprehensively investigated using first-principles calculations. Firstly, to elucidate how symmetry breaking in BK lattice modifies the electronic structure, the normal kagome (NK) lattice (right side of Figure 1c), analogous to the Co-kagome lattice in $Co_3Sn_2S_2$ [5], is considered. Figure 1d presents the orbital projection of the band structures along the high-symmetry paths for BK lattice, together with the band structures with spin-orbit coupling (SOC) for NK lattice. Relative to NK lattice, the linear band crossings for the BK lattice shift closer to E_F along the Γ-A-L directions. Meanwhile, these crossings become broadened and split in energy, such that the six Weyl-node pairs for NK lattice evolve into twelve pairs for BK lattice (Figure 1e). Besides, a clear band crossing happens along the Γ-H path in BK lattice. These comparisons demonstrate that symmetry breaking in BK lattice produces a richer manifold of topological electronic states. In addition, the orbital analysis further indicates that the Cr_*d* and Ge_*p* states dominate the bands near E_F, suggesting that the charge carriers move in a BK-hybridized Cr-Ge layer, consistent with the transport scenario proposed in Figure 1a.

Then, the topological states of $LaCrGe_3$ with BK lattice were explored. Without considering SOC, the spin-up channels intersect with spin-down channels, forming linear band crossings that trace out nodal rings lying in the plane (Figure 1d,f; Figures S4 and S5). After turning on SOC, the two spin channels couple together, then the relevant mirror symmetries are broken with the magnetization along *c*-axis direction. Consequently, the nodal rings are gapped, while three pairs of Weyl points remain along the Γ-M direction and one pair survives along the Γ-K direction (Figure 1g). Specifically, the nodal rings that were previously protected by the M_{110} mirror plane evolve into two Weyl pairs (WP2 and WP3). The Weyl pair labeled as WP1 along the Γ-K direction remains associated with the ring protected by the glide-mirror plane $\tilde{\mathcal{M}}_{1-10}$, whereas an additional pair (WP4) appears outside the nodal rings due to an accidental band degeneracy (Figure 1f). All four types of Weyl points identified within the energy window from -150 to 100 meV are classified as Type-I Weyl points. Figure 1g summarizes the distribution of these Weyl points in $k_{x\text{-}y}$ plane within this energy window, taking the C_{3z} rotation symmetry into account (see the location information of Weyl points in *k*-space in Table S1). The Weyl points with opposite chirality are related by inversion symmetry. Moreover, the gapped nodal rings generate a pronounced Berry curvature, which dominates the transport phenomena, including a large intrinsic anomalous Hall conductivity.

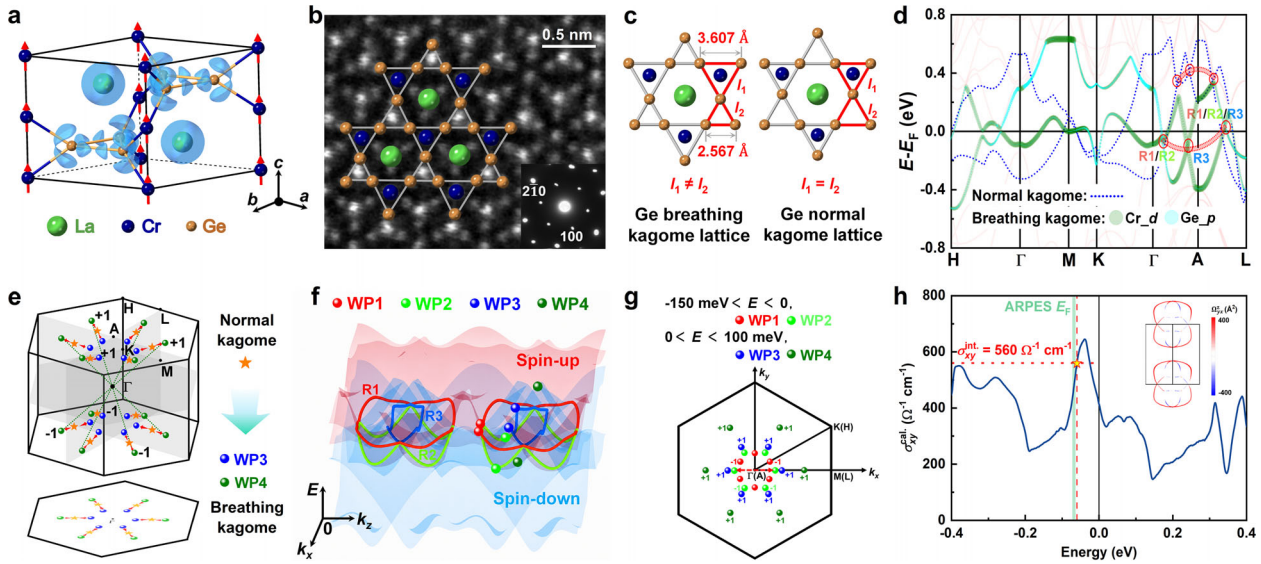

FIGURE 1 | Crystal, kagome lattice, electronic band structure, topological states, and Fermi level. (a) Crystal and magnetic structures of $LaCrGe_3$, together with the three-dimension electron localization function (ELF). The isosurface value is 0.77 e Bohr^{-3}. (b) High resolution transmission electron microscope (HRTEM) images of $LaCrGe_3$. The Ge atoms form a breathing kagome (BK) lattice. The inset shows the electron-diffraction pattern taken along *c*-axis. (c) Schematic diagrams of BK lattice and the normal kagome (NK) lattice. The BK lattice consists of corner-sharing triangles in which two inequivalent triangles with different side lengths ($l_1 \neq l_2$) alternate, whereas NK lattice consists of corner-sharing triangles with $l_1 = l_2$. d, Energy dispersion of electronic bands along high-symmetry paths of BK and NK lattice with spin-orbit coupling (SOC) near the Fermi level (E_F). The Cr_*d* and Ge_*p* orbitals resolved the electronic band structures for BK lattice. The linear band crossings along the Γ-A-L direction correspond to nodal rings 1/2 (R1/R2), nodal ring 3 (R3) and nodal rings 1/2/3 (R1/R2/R3), respectively. (e) Weyl points of BK and NK lattices. The three-dimensional Brillouin zone with high-symmetry points shows 12 pairs of Weyl points for BK lattice (blue and green spheres) and six pairs for NK lattice (orange stars). (f) Band crossings from the spin-up and spin-down channels form three nodal rings (R1-R3) in $k_{x\text{-}z}$ plane, together with the geometric relationship between Weyl points and nodal rings. Notably, WP4 appears outside the nodal rings, which is an incidental occurrence. (g) Distribution of Weyl points in $k_{x\text{-}y}$ plane over the energy range of -150 to 100 meV. The Weyl points can be classified into two categories: WP1 and WP2 lie below E_F, whereas WP3 and WP4 lie above E_F. WP2 is observed by ARPES (marked by red arrows). h, Energy dependence of the theoretically calculated anomalous Hall conductivity ($\sigma_{xy}^{cal.}$). At E = -60 meV, $\sigma_{xy}^{cal.} = 560\ \Omega^{-1}\ cm^{-1}$, which is mainly contributed by the Berry curvature of the nodal lines as shown in the inset.

To elucidate the influence of topological band structures on transverse transport, the measurements of Hall resistivity (ρ_{yx}) were performed (see Figure S12). The anomalous Hall conductivity (σ_{xyA}) reaches a maximum value of ~ 700 Ω^{-1} cm^{-1} at 2 K. Furthermore, using the TYJ scaling model [28], the intrinsic anomalous conductivity ($\sigma_{xy}^{int.}$) is extracted to be 560 Ω^{-1} cm^{-1} (see Figure S13). As shown in Figure 1h, the corresponding $\sigma_{xy}^{int.}$ can be found in positions slightly below E_F. Combined this with the E_F position determined by ARPES, E_F of the transport-measured sample should be shifted downward by ~ 60 meV. The shift can be attributed to slight lack of Ge revealed by the energy dispersive x-ray spectroscopy (EDS) (see Section S1). The inset of Figure 1k highlights the strong Berry curvature, which mainly originates from the gapped topological nodal lines. Overall, the large anomalous Hall effect observed experimentally supports the theoretical predictions and evidences the topological nature of $LaCrGe_3$.

Further, the electronic structures of $LaCrGe_3$ were measured at 23 K on the (100) surface (Figure 2a), and the observed band structures agree well with the theoretical calculations, as shown in Figure 2b–f. The Fermi surface of $LaCrGe_3$ around the Γ point in Figure 2b exhibits hourglass-like shape, which can be reproduced by the theoretical calculations in Figure 2c. The experimental band dispersions are also consistent with the calculations as shown in Figure 2d,e, featuring an electron pocket along the M-Γ-M direction and a hole pocket along the L-M-L direction. Moreover, a linear dispersion is observed along M'-H'-M' direction, as indicated by the red dashed lines in left panel of Figure 2f. Such linear dispersions forms Weyl points (WP2) as demonstrated by the calculations in right panel of Figure 2f, and the corresponding positions in BZ are indicated in Figure 2b,c. The temperature-dependent ARPES measurements indicate that $LaCrGe_3$ undergoes a topological phase transition with clear band splitting across the magnetic transition (see Figure S7). In addition, as shown in Figure 2d, the calculated flat band around -0.5 eV is not clearly resolved in the ARPES spectra. This may be due to photoemission matrix-element effects, as the spectral weight of a band depends on photon polarization and energy, photoelectron momentum, experimental geometry, and orbital parity [29, 30]. Since the Weyl points discussed here are located near the Fermi level, this does not affect the identification of the Weyl electronic structure relevant to the present work. The observation of bulk Weyl points with linear dispersions establishes $LaCrGe_3$ as a magnetic Weyl semimetal.

3 | Spin-Rotation Modulated Weyl–Fermion Motion

As a newly established magnetic Weyl semimetal, $LaCrGe_3$ provides a versatile platform for exploring topological states

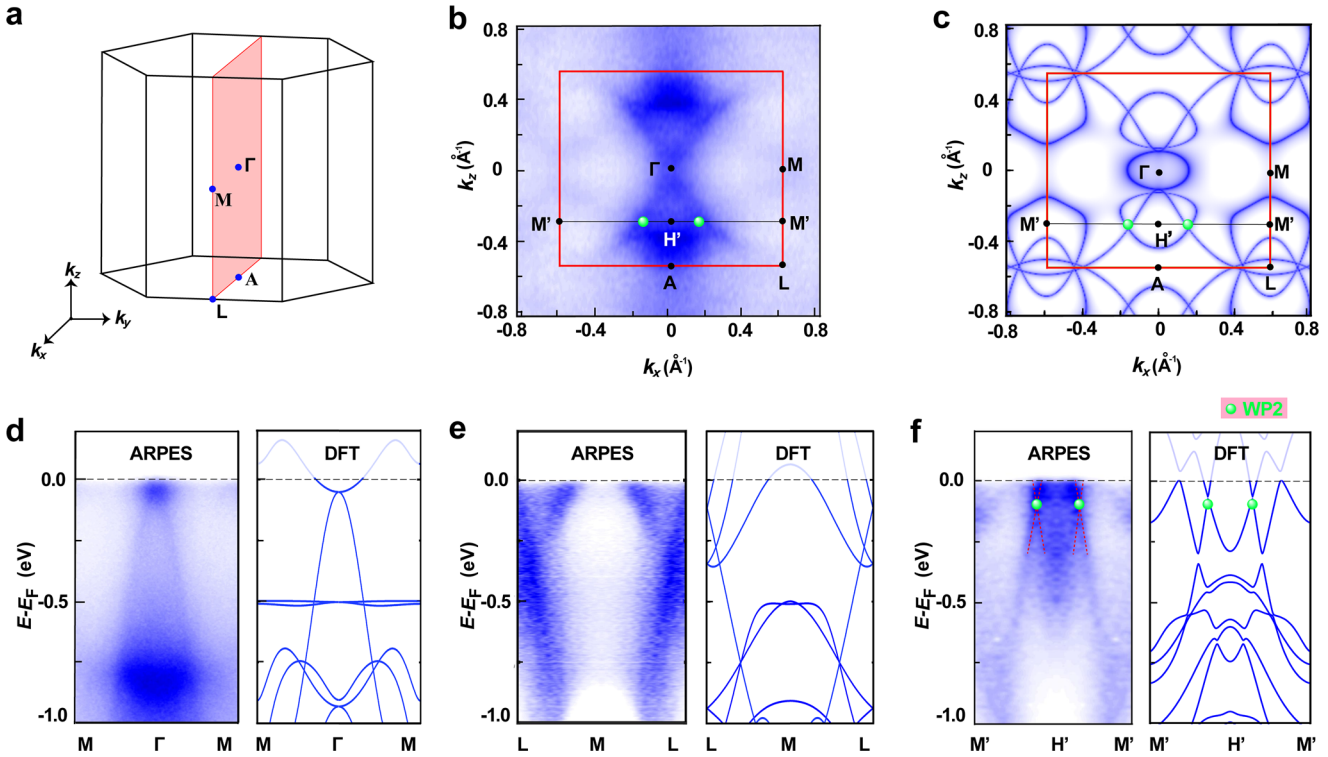

FIGURE 2 | ARPES evidence of Weyl topological state. (a) Bulk Brillouin zone (BZ) with high-symmetry points. (b and c) Experimental and calculated Fermi surface on the (100) surface, respectively. The bright green dots mark the position of the Weyl points (WP2) in BZ. (d–f) Comparison of experimental (left panel) and calculated (right panel) band structures along different high-symmetry directions. The Weyl points (WP2) are observed as shown in (f) indicated by the bright green dots, and the red dashed lines are the eye-guide lines for the linear dispersion of Weyl bands. Notably, the experimental E_F of samples is shifted downward by ~ 67 meV compared to the theoretical calculations, accordingly, and all calculated band diagrams in (d–f) have thus been processed by applying a corresponding downward shift to E_F. The shift value is highly consistent with that determined by the transport measurements (Figure 1h).

and their associated physical properties. Considering that the saturation field of $LaCrGe_3$ in the hard axis is only ~ 4 T, it is possible to rotate the magnetic moments to modulate the electronic bands and track the evolution of topological states, and the theoretical calculations can further be used to predict the related signatures. Figure 3a summarizes the distribution of Weyl points in three-dimensional (3D) Brillouin zone for M // c and M // ab. When the magnetic moment rotates from c - axis to ab - plane, as shown in Figure 3b, WP2 near the Γ point annihilates first, followed by the annihilation of WP1 at small magnetization angles ($\alpha < 15°$). Notably, WP1 and WP2 approach to E_F at $\alpha = 5°$. With further increasing α, WP3 and WP4 move toward E_F, reaching their minimum in energy at $\alpha = 45°$, yet keeping above E_F during the whole magnetization rotation. In particular, WP4 survives throughout the rotation, highlighting its robustness, as it represents an accidental degeneracy point devoid of any symmetry protection in this system. The evolution of WP1-WP4 in k-space position is demonstrated in Figure 3c, consistent with their energy evolution. The insets of Figure 3c further indicate that WP1, WP2, and WP3 migrate along 3D steep dispersion nodal lines during the rotation process. WP4, without any protection of symmetry, does not follow the trajectory along the nodal line.

The spin-orientation-dependent evolution of the Weyl electronic structure predicted above can be indirectly probed by the angle-dependent magnetoresistance. As shown in Figure 3d, a positive, unsaturated magnetoresistance is observed at $T = 2$ K when B is perpendicular to I ($\theta = 0°$), and its sign gradually changes from positive to negative as θ increases. For B parallel I ($\theta = 90°$), the corresponding positive magnetoconductance is shown in Figure 3e, providing an equivalent representation of the negative magnetoresistance. Since there is a horizontal component of the connection between chirality-opposite Weyl pairs in ab-plane (Figure 3a), the negative magnetoresistance consistent with a chiral-anomaly-related contribution can occur, which originates from an additional contribution to the conductivity from chiral charge pumping, arising from the non-conservation of chiral charge under parallel magnetic and electric fields [31, 32]. Accordingly, as depicted in the inset of Figure 3e, when B // ab at low fields, the magnetic moments tend to be arranged close to c-axis (the easy axis), and the magnetoconductance follows an approximately parabolic field dependence (~ B^2), which is consistent with the semiclassical behavior expected for a chiral-anomaly-related contribution and with the calculated presence of WP1 and WP2 in the corresponding magnetic configuration [31, 33]. As B increases, α increases and the field dependence gradually deviates from the parabolic form, suggesting a modification of the Weyl-related transport response associated with the calculated evolution of Weyl points and Berry curvature. In particular, for $B > 4$ T, the magnetic moments are completely arranged along a-axis where the rotational symmetry is reduced from threefold to twofold, leading to a calculated change in the topological electronic states, as shown in Figure 3a–c. In this high-field

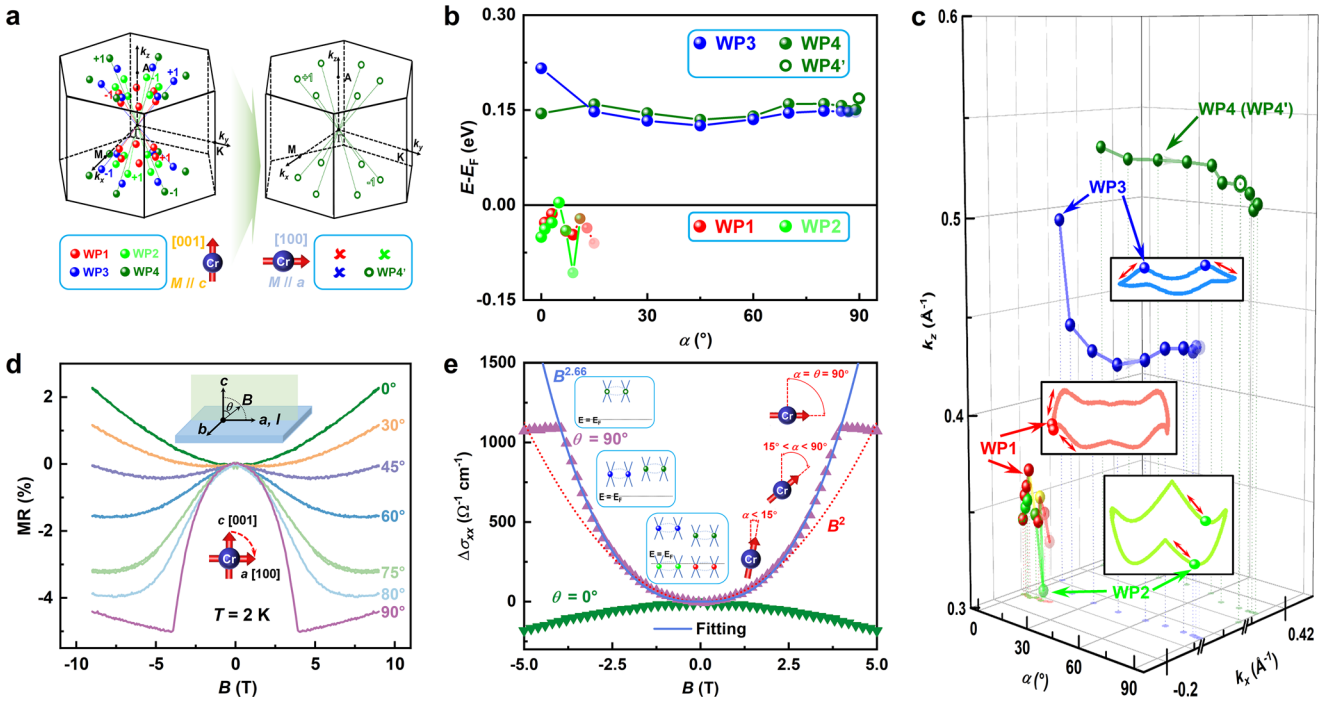

FIGURE 3 | Spin-rotation driven Weyl fermion motion. (a) Distribution of Weyl points in 3D BZ with the magnetic moments aligned along *c*-axis and *a*-axis. As the magnetic moments rotate from *c*-axis to *a*-axis, WP1-WP3 annihilate whereas only WP4 (WP4') survives. (b) Energies of Weyl points as a function of the magnetization angle α (defined as the angle the angle by which the magnetic moments deviate from *c*-axis) with shifted E_F. WP1 and WP2 annihilate after $\alpha = 15°$ and 11°, respectively, and WP3 annihilates at $\alpha = 90°$. (c) Positions (k_x and k_z) of WP1-WP4 as a function of α, with the moving rings of WP1-WP3 under different symmetry protections. (d) Angle dependence of magnetoresistance at 2 K. The magnetoresistance rapidly drops with increasing θ, where θ denotes the angle between the magnetic field and *c*-axis. The upper inset shows a schematic of the measurement geometry, and the lower inset indicates the rotation of the magnetic moment from *c*-axis to *a*-axis. (e) Magnetoconductance at 2 K for both $B \perp I$ and $B // I$. The red-dashed fit shows a B^2 dependence of the positive magnetoconductance at low fields for $B // I$, consistent with a chiral-anomaly-related contribution in the corresponding Weyl state. The blue fit yields a $B^{2.66}$ dependence at $B < 4$ T, indicating a deviation from the simple parabolic behavior, which is associated with magnetic-field-induced spin reorientation and the calculated evolution of the Weyl electronic structure. The insets schematically illustrate the calculated evolution of Weyl points during this process.

regime, the spin-dependent scattering weakened by the *ab*-plane magnetic order, becomes the dominant contribution, accounting for the pronounced deviation of the experimental curve from the standard B^2 behavior. Overall, these magnetoconductance trends serve as indirect evidence supporting the calculated spin-orientation-dependent evolution of the Weyl electronic structure.

4 | Spin-Rotation Modulated Transverse Transport Evolution

The evolution of topological states during the rotation of moments drastically modifies the Berry curvature Ω^z_{xy} in *k*-space. The insets of Figure 4a illustrate the corresponding changes in Ω^z_{xy} associated with the nodal lines. Specifically, at $\alpha = 0°$, Ω^z_{xy} is dominated by positive contributions. At $\alpha = 45°$, both the positive and negative components become enhanced, resulting in a modest drop in the net value. When α increases to 90°, the magnitudes of both components diminish, driving the net Ω^z_{xy} toward zero. As a result, the integration of Ω^z_{xy} decreases gradually for $\alpha < 45°$ but drops rapidly for $\alpha > 45°$, as illustrated in Figure 4a (see details in Figure S5). In particular, the Berry curvature generated by WP4 is clearly visible outside the nodal rings, particularly at $\alpha = 90°$.

The electronic bands also evolve during this process. We present the representative bands along the Γ-A direction at different rotation angles α, as shown in Figure 4b. As α increases, the upper and lower bands on the left progressively approach each other and eventually become fully degenerate at $\alpha = 90°$. In details, the energy gap (ΔE) between these two bands gradually decreases with increasing α and vanishes at $\alpha = 90°$, as illustrated in Figure 4c. These results indicate that band degeneracy develops on the left side along the Γ-A direction, leading to a suppression of the corresponding Berry curvature. By contrast, for the bands on the right along the Γ-A direction, the crossing remains largely unchanged. Consequently, the Berry curvature generated by the crossing is essentially negligible and shows little dependence on α (see Figure S5).

The intrinsic anomalous Hall conductivity is a measurable quantity directly linked to the Berry curvature. Accordingly, the further measurements of field dependence of σ_{xy} at different rotating angles were carried out, as shown in Figure 4e. Interestingly, the curves display a cusp-like feature when θ ranges from 45° to 90°. During this rotating process, σ^A_{xy} is determined by the Berry curvature component Ω^z_{xy}, which is related to M_z, as illustrated in the inset of Figure 4d. Taking $\theta = 87.5°$ as an example (Figure 4d), the system is in a multi-domain state at zero field, yielding a vanishing net magnetization. As *B* increases,

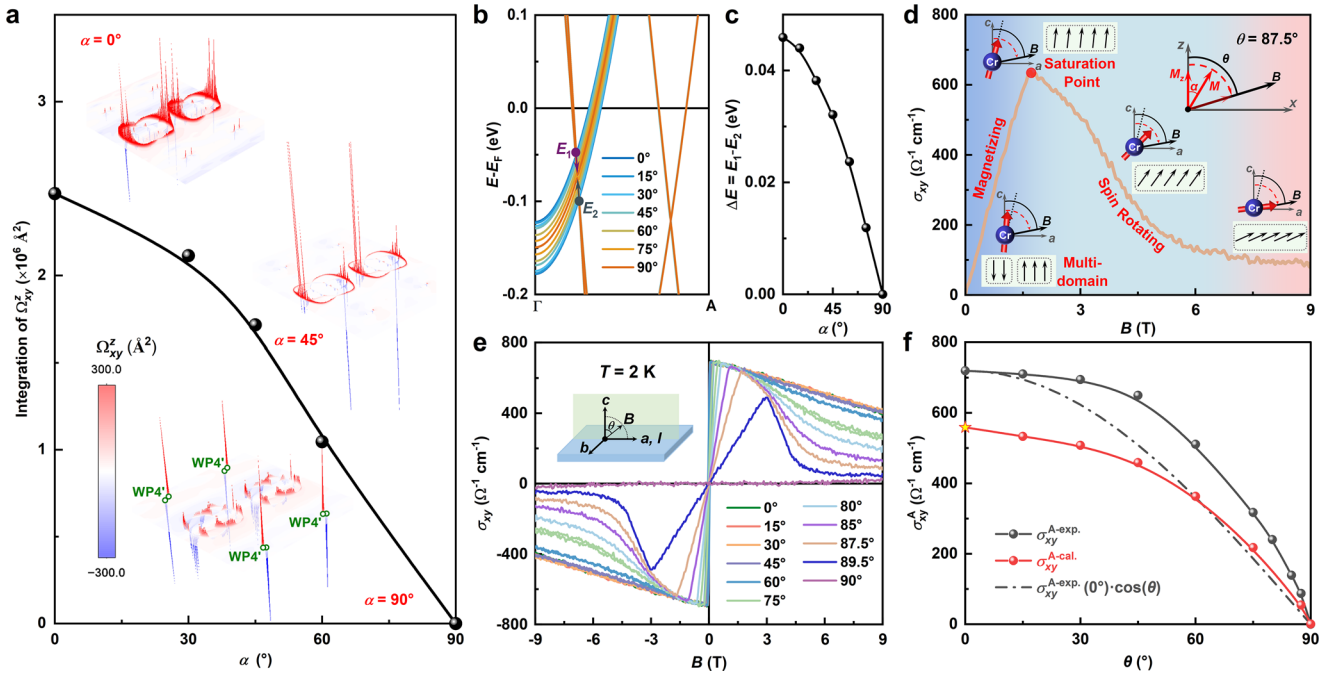

FIGURE 4 | Spin-rotation driven transport evolution. (a) Angle dependence of the integration of Berry curvature Ω_{xyz} below E_F in k-space. The insets show the Berry-curvature distribution of the nodal lines at $\alpha = 0°$, 45° and 90°. Beyond the nodal rings, WP4 contributes a notably significant Berry curvature. (b) Evolution of electronic bands along the Γ-A direction during the rotation of magnetic moment. E_1 and E_2 correspond to the energies of the linear crossings on the two leftmost bands, respectively. The crossings on the left correspond to SOC-gapped R1/2, and the crossings on the right correspond to SOC-gapped R3. (c) Angle dependence of the energy difference between E_1 and E_2 in (b). (d) Physical illustration of the relationship between the magnetization process and unconventional transport behavior, with $\theta = 87.5°$ as an example. The insets show the process in which the magnetic moments change from multi domains to a single domain by magnetizing and then rotate toward the direction of the magnetic field. After the magnetic order stabilizes, $\alpha = \theta$. (e) Field dependence of Hall conductivity from 0° to 90°. An unconventional transport behavior is observed, where a cusp-like feature appears in the curves when θ is between 45° to 90°. The inset shows the configuration schematic diagram of the sample geometry. (f) Angle dependence of anomalous Hall conductivity σ^{A}_{xy} for both the calculation and experiment. The dash dots indicate the dependence of $\sigma^{A-exp.}_{xy} \cdot \cos\theta$. The yellow star represents the experimentally determined intrinsic value, which is consistent with theoretical calculations at E = -60 meV.

the multiple domains gradually evolve into a single domain, and the moments reach the saturation where M_z attains its maximum. With further increasing B, the moments rotate toward the field direction, causing M_z to decrease progressively. Once M becomes fully aligned with B, the rotation of moments ceases and M_z reaches a constant value. Thus, during the evolution from domain alignment to spin rotation, M_z first increases to a maximum and then decreases to a constant value, consistent with the variation of the Hall signal. This correspondence indicates that the cusp-like feature originates from the anomalous Hall effect rather than from a topological Hall contribution. Therefore, the observed anomalous Hall behavior can be consistently understood based on the above calculations (Figures 3b and 4a). At low B, α is small and the topological states are not altered, so σ^{A}_{xy} exhibits a large value. However, further increasing B, the moments deviate significantly from c-axis, driving the annihilation of the topological states and causing a pronounced change in σ^{A}_{xy}. At high fields, M becomes fully aligned with B, and the rotation stops. Consequently, the electronic band structure of $LaCrGe_3$ stabilizes, resulting in a constant σ^{A}_{xy}. It can be noted that the magnetization direction modifies σ^{A}_{xy} due to the breaking of mirror symmetry and appreciable changes in some bands.

Furthermore, after the magnetic moments align along the magnetic field direction ($\alpha = \theta$), the angle-dependent $\sigma^{A-exp.}_{xy}$ can be extracted at different θ by high-field extrapolation of the data in Figure 4e. Figure 4f depicts the angle dependence of $\sigma^{A-exp.}_{xy}$ and $\sigma^{A-cal.}_{xy}$, and the two curves exhibit a similar changing trend where the values of σ^{A}_{xy} remains nearly constant from 0° to 45°, followed by a rapid decrease from 45° to 90°, consistent with the evolution of Ω^{z}_{xy} in Figure 4a. Clearly, the angle dependence deviates from a simple $\cos\theta$ behavior, indicating that the variation originates from the evolution of the electronic band structure rather than a purely geometric projection effect.

5 | Conclusion

In summary, our theoretical and experimental work collectively establish $LaCrGe_3$ as a magnetic Weyl semimetal. The prediction is confirmed by direct ARPES observation of bulk Weyl points and by transport evidence, including the large anomalous Hall conductivity and chiral-anomaly-related negative magnetoresistance. Based on the magnetic anisotropy of $LaCrGe_3$, we further regulated the topological states by reorienting the magnetic moments in rotating magnetic fields, which successfully enables the realizations of Weyl fermion motion and electronic transport evolution. The feasible external-field modulation of topological states and electronic transport provides important indications to

the frontier developments of topological spintronics and quantum devices.

6 | Methods

6.1 | Single Crystal Growths

The single crystals of $LaCrGe_3$ were grown by Ge self-flux method [34, 35]. First, a mixture of La, Cr, and Ge was premixed with a molar ratio of 13:13:74 by arc melting. Then the mixture was placed in an alumina crucible and sealed in a quartz tube under partial pressure of high purity Argon gas. The quartz tube was heated to 1100°C in 12 h and kept it for 24 h, then slowly cooled to 850°C over one week. Finally, the remaining liquid was decanted using a centrifuge to obtain $LaCrGe_3$ single crystals which exhibit hexagonal shape (see Figure S1).

6.2 | Composition Characterizations

The chemical compositions of crystals were performed on a Hitachi S-4800 scanning electron microscope (SEM) with the energy dispersive x-ray spectroscopy (EDS).

6.3 | Structural Characterizations

Before transmission electron microscope (TEM) analysis, the single crystalline foils were cut from the bulk crystal using the focused ion beam (FIB) and then transferred to the copper grid. High-resolution high-angle annular dark field images and selected area electron diffraction patterns were acquired in JEOL ARM200F transmission electron microscope equipped with cold field-emission gun and double Cs correctors.

6.4 | Magnetization Measurements

The magnetic properties of $LaCrGe_3$ single crystals were measured in the vibrating sample magnetometer of Physical Property Measurement System (PPMS-9, Quantum Design), with the magnetic field rotated from *c*-axis to *a*-axis.

6.5 | Transport Measurements

The longitudinal and Hall resistivities were measured using the DC Resistivity Option of PPMS-9. The rotation measurements were performed using the horizontal rotator option of PPMS-9. The measured samples were cut and grinded to form rectangular slices and the four-probe method was used (see Figure S9). The reliability of the computational formula of σ_{xy}^{A} has been demonstrated during the rotating moments (see Figure S6 and Section S6.4).

6.6 | ARPES Measurements

Synchrotron-based ARPES measurements were conducted under ultra-high vacuum (UHV) better than 1×10^{-10} mbar at Shanghai Synchrotron Radiation Facility (SSRF) and Synchrotron SOLEIL. The measurements were performed from 10 to 100 K with a photon energy of 90 and 142 eV. The data were collected with a Scienta DA30L electron analyzer. The total energy and angular resolutions were set to 20 meV and 0.2°, respectively.

6.7 | Theoretical Calculations

First-principles calculations based on the density-functional theory (DFT) were performed using the projector-augmented wave (PAW) method [36] as implemented in the Vienna ab initio simulation package (VASP) [37]. The generalized gradient approximation (GGA) of Perdew–Burke–Ernzerhof (PBE) [38] for the exchange-correlation functional was used. The cut-off energy of plane wave basis was set 550 eV and the first Brillouin zone of the reciprocal space was sampled with the Γ-centered *k*-point meshes. The structure was fully relaxed until the force, and energy is smaller than 0.001 eV/Å and 10^{-6} eV. The Cr_*d* and Ge_*p* orbitals were used to construct the tight-binding model with the maximally localized Wannier functions (MLWF) by Wannier90 code [39]. Using the obtained tight-binding models, energy dependence of the anomalous Hall conductivity (AHC) σ_{xy}^{z} in terms of the *z* components of Berry curvature was obtained by the WannierBerri code [40]. The Wanniertools package [41] was used to find the Weyl points and calculate Berry curvature.

Author Contributions

E.L. conceived and supervised the project. Y.L. synthesized the crystals, carried out the XRD and EDS measurements, and performed the magnetic and transport measurements. J.L. performed the theoretical calculations. J.M. and D.L. conducted the ARPES measurements. Y.Y. performed the HRTEM measurements. Y.L., J.L., J.M., J.Y., M.L., Y.W., S.S., X.D., X.Liu., B.W., X.Li., C. F., D.L. and E.L. analyzed and discussed the experimental data. Y.L., J.L. and E.L. wrote this manuscript with input from all authors.

Acknowledgements

This work was supported by the Strategic Priority Research Program (B) of the Chinese Academy of Sciences (CAS) (No. XDB1720000), the National Key R&D Program of China (No. 2022YFA1403800), the National Natural Science Foundation of China (Nos. 12595332, 52331008, and 12374454), the Synergetic Extreme Condition User Facility (SECUF), and China-Germany Joint Research Center on Quantum Materials and Physics under Extreme Conditions.

Conflicts of Interest

The authors declare no conflicts of interest.

Data Availability Statement

The data that support the findings of this study are available from the corresponding author upon reasonable request.

References

1. Y. Tokura, K. Yasuda, and A. Tsukazaki, "Magnetic Topological Insulators," *Nature Reviews Physics* 1 (2019): 126–143, https://doi.org/10.1038/s42254-018-0011-5.

2. Q. L. He, T. L. Hughes, N. P. Armitage, Y. Tokura, and K. L. Wang, "Topological Spintronics and Magnetoelectronics," *Nature Materials* 21 (2022): 15–23, https://doi.org/10.1038/s41563-021-01138-5.

3. M. Zhong, N. T. T. Vu, W. Zhai, et al., "Weyl Semimetals: From Principles, Materials to Applications," *Advanced Materials* 37 (2025): 2506236, https://doi.org/10.1002/adma.202506236.

4. H. Weng, C. Fang, Z. Fang, B. A. Bernevig, and X. Dai, "Weyl Semimetal Phase in Noncentrosymmetric Transition-Metal Monophosphides," *Physical Review X* 5 (2015): 011029, https://doi.org/10.1103/PhysRevX.5.011029.

5. E. Liu, Y. Sun, N. Kumar, et al., "Giant Anomalous Hall Effect in a Ferromagnetic Kagome-Lattice Semimetal," *Nature Physics* 14 (2018): 1125–1131, https://doi.org/10.1038/s41567-018-0234-5.

6. I. Belopolski, K. Manna, D. S. Sanchez, et al., "Discovery of Topological Weyl Fermion Lines and Drumhead Surface States in a Room Temperature Magnet," *Science* 365 (2019): 1278–1281, https://doi.org/10.1126/science.aav2327.

7. A. Sakai, Y. P. Mizuta, A. A. Nugroho, et al., "Giant Anomalous Nernst Effect and Quantum-Critical Scaling in a Ferromagnetic Semimetal," *Nature Physics* 14 (2018): 1119–1124, https://doi.org/10.1038/s41567-018-0225-6.

8. S. Guin, P. Vir, and Y. Zhang, "Zero-Field Nernst Effect in a Ferromagnetic Kagome-Lattice Weyl-Semimetal $Co_3Sn_2S_2$," *Advanced Materials* 31 (2019): 1806622, https://doi.org/10.1002/adma.201806622.

9. F. L. Zeng, Z. Y. Ren, Y. Li, et al., "Intrinsic Mechanism for Anisotropic Magnetoresistance and Experimental Confirmation in Co_xFe_{1-x} Single-Crystal Films," *Physical Review Letters* 125 (2020): 097201, https://doi.org/10.1103/PhysRevLett.125.097201.

10. D. F. Liu, A. J. Liang, E. K. Liu, et al., "Magnetic Weyl Semimetal Phase in a Kagomé Crystal," *Science* 365 (2019): 1282–1285, https://doi.org/10.1126/science.aav2873.

11. J. Shen, Q. Zeng, and S. Zhang, "On the Anisotropies of Magnetization and Electronic Transport of Magnetic Weyl Semimetal $Co_3Sn_2S_2$," *Applied Physics Letters* 116 (2020): 212403, https://doi.org/10.1063/1.5125722.

12. K. Nakazawa, Y. Kato, and Y. Motome, "Topological Transitions by Magnetization Rotation in Kagome Monolayers of the Ferromagnetic Weyl Semimetal Co-Based Shandite," *Physical Review B* 110 (2024): 085112, https://doi.org/10.1103/PhysRevB.110.085112.

13. K. Kuroda, T. Tomita, M.-T. Suzuki, et al., "Evidence for Magnetic Weyl Fermions in a Correlated Metal," *Nature Materials* 16 (2017): 1090–1095, https://doi.org/10.1038/nmat4987.

14. Y. Song, Y. Hao, S. Wang, et al., "Complicated Magnetic Structure and Its Strong Correlation with the Anomalous Hall Effect in Mn_3Sn," *Physical Review B* 101 (2020): 144422, https://doi.org/10.1103/PhysRevB.101.144422.

15. P. Li, J. Koo, W. Ning, et al., "Giant Room Temperature Anomalous Hall Effect and Tunable Topology in a Ferromagnetic Topological Semimetal Co_2MnAl," *Nature Communications* 11 (2020): 3476, https://doi.org/10.1038/s41467-020-17174-9.

16. S. Kumar, S. Sarkar, and S. C. Peter, "Diversity in Crystal Structure and Physical Properties of $RETX_3$ (*RE*-Rare Earth, *T*-Transition Metal, *X*-Main Group Element) Intermetallics," *Chemical Record* 22 (2022): 202100317, https://doi.org/10.1002/tcr.202100317.

17. W. Bazela, "The Influence of the Crystal Structure on the Magnetic Ordering in RT_2X_2 and RTX_3 Compounds," *Journal of Alloys and Compounds* 442 (2007): 132–135, https://doi.org/10.1016/j.jallcom.2006.08.349.

18. V. Anand, D. Adroja, and A. Hillier, "Ferromagnetic Cluster Spin-Glass Behavior in $PrRhSn_3$," *Physical Review B* 85 (2012): 014418, https://doi.org/10.1103/PhysRevB.85.014418.

19. H. Yamamoto, M. Ishikawa, K. Hasegawa, and J. Sakurai, "$CeFeGe_3$: A Concentrated Kondo Compound with a Stable Valency and High Kondo Temperature," *Physical Review B* 52 (1995): 10136–10141, https://doi.org/10.1103/PhysRevB.52.10136.

20. A. P. Pikul, D. Kaczorowski, T. Plackowski, et al., "Kondo Behavior in Antiferromagnetic $CeNiGe_3$," *Physical Review B* 67 (2003): 224417, https://doi.org/10.1103/PhysRevB.67.224417.

21. K. Ghosh, S. Ramakrishnan, S. K. Dhar, et al., "Crystal Structures and Low-Temperature Behaviors of the Heavy-Fermion Compounds $CeRuGe_3$ and $Ce_3Ru_4Ge_{13}$ Containing Both Trivalent and Tetravalent Cerium," *Physical Review B* 52 (1995): 7267–7277, https://doi.org/10.1103/PhysRevB.52.7267.

22. N. Kimura, K. Ito, K. Saitoh, Y. Umeda, H. Aoki, and T. Terashima, "Pressure-Induced Superconductivity in Noncentrosymmetric Heavy-Fermion $CeRhSi_3$," *Physical Review Letters* 95 (2005): 247004, https://doi.org/10.1103/PhysRevLett.95.247004.

23. M. Feig, M. Nicklas, M. Bobnar, et al., "Superconductivity and Magnetism in Noncentrosymmetric $LaPtGe_3$ and $CePtGe_3$," *Physical Review B* 98 (2018): 184516, https://doi.org/10.1103/PhysRevB.98.184516.

24. F. R. Arantes, D. Aristizábal-Giraldo, D. A. Mayoh, et al., "Superconductivity in Monocrystalline $YNiSi_3$ and $LuNiSi_3$," *Physical Review B* 99 (2019): 224505, https://doi.org/10.1103/PhysRevB.99.224505.

25. L. Li, S. Guan, S. Chi, et al., "Giant Anomalous Hall and Nernst Effects in a Heavy Fermion Ferromagnet," *Science Bulletin* 71 (2026): 2463–2472, https://doi.org/10.1016/j.scib.2026.04.027.

26. Z. Yu, H. You, X. Luo, et al., "Large Anomalous Hall Effect Induced by Skew Scattering in the Hexagonal Ferromagnet $PrCrGe_3$," *Physical Review B* 111 (2025): 125112, https://doi.org/10.1103/PhysRevB.111.125112.

27. H. Bie, O. Y. Zelinska, A. V. Tkachuk, and A. Mar, "Structures and Physical Properties of Rare-Earth Chromium Germanides $RECrGe_3$ (*RE* = La–Nd, Sm)," *Chemistry of Materials* 19 (2007): 4613–4620, https://doi.org/10.1021/cm071276.

28. Y. Tian, L. Ye, and X. Jin, "Proper Scaling of the Anomalous Hall Effect," *Physical Review Letters* 103 (2009): 087206, https://doi.org/10.1103/PhysRevLett.103.087206.

29. A. Damascelli, Z. Hussain, and Z. X. Shen, "Angle-Resolved Photoemission Studies of the Cuprate Superconductors," *Reviews of Modern Physics* 75 (2003): 473–541, https://doi.org/10.1103/RevModPhys.75.473.

30. S. Moser, "An Experimentalist's Guide to the Matrix Element in Angle Resolved Photoemission," *Journal of Electron Spectroscopy and Related Phenomena* 214 (2017): 29–52, https://doi.org/10.1016/j.elspec.2016.11.007.

31. D. Son and B. Spivak, "Chiral Anomaly and Classical Negative Magnetoresistance of Weyl Metals," *Physical Review B* 88 (2013): 104412, https://doi.org/10.1103/PhysRevB.88.104412.

32. A. Burkov, "Chiral Anomaly and Transport in Weyl Metals," *Journal of Physics: Condensed Matter* 27 (2015): 113201, https://doi.org/10.1088/0953-8984/27/11/113201.

33. N. Ong and S. Liang, "Experimental Signatures of the Chiral Anomaly in Dirac–Weyl Semimetals," *Nature Reviews Physics* 3 (2021): 394–404, https://doi.org/10.1038/s42254-021-00310-9.

34. X. Lin, V. Taufour, S. L. Bud'ko, and P. C. Canfield, "Suppression of Ferromagnetism in the $LaV_xCr_{1-x}Ge_3$ System," *Physical Review B* 88 (2013): 094405, https://doi.org/10.1103/PhysRevB.88.094405.

35. U. Kaluarachchi, S. Bud'ko, and P. Canfield, "Tricritical Wings and Modulated Magnetic Phases in $LaCrGe_3$ under Pressure," *Nature Communications* 8 (2017): 546, https://doi.org/10.1038/s41467-017-00699-x.

36. P. Blochl, "Projector Augmented-Wave Method," *Physical Review B* 50 (1994): 17953–17979, https://doi.org/10.1103/PhysRevB.50.17953.

37. G. Kresse and J. Furthmuller, "Efficiency of Ab-Initio Total Energy Calculations for Metals and Semiconductors Using a Plane-Wave Basis Set," *Computational Materials Science* 6 (1996): 15–50, https://doi.org/10.1016/0927-0256(96)00008-0.

38. J. Perdew, K. Burke, and M. Ernzerhof, "Generalized Gradient Approximation Made Simple," *Physical Review Letters* 77 (1996): 3865–3868, https://doi.org/10.1103/PhysRevLett.77.3865.

39. A. A. Mostofi, J. R. Yates, Y.-S. Lee, I. Souza, D. Vanderbilt, and N. Marzari, "Wannier90: A Tool for Obtaining Maximally-Localised Wannier Functions," *Computer Physics Communications* 178 (2008): 685–699, https://doi.org/10.1016/j.cpc.2007.11.016.

40. S. Tsirkin, "High Performance Wannier Interpolation of Berry Curvature and Related Quantities with WannierBerri Code," *npj Computational Materials* 7 (2021): 33, https://doi.org/10.1038/s41524-021-00498-5.

41. Q. Wu, S. Zhang, H.-F. Song, M. Troyer, and A. A. Soluyanov, "WannierTools: An Open-Source Software Package for Novel Topological Materials," *Computer Physics Communications* 224 (2018): 405–416, https://doi.org/10.1016/j.cpc.2017.09.033.

Supporting Information

Additional supporting information can be found online in the Supporting Information section.

Supporting File: adma74402-sup-0001-SuppMat.docx.